metals

Article

Genetic Algorithm-Based Framework for Optimization of Laser Beam Path in Additive Manufacturing

Primož Potočnik *, Andrej Jeromen and Edvard Govekar

Faculty of Mechanical Engineering, University of Ljubljana, Aškerčeva 6, SI-1000 Ljubljana, Slovenia; andrej.jeromen@fs.uni-lj.si (A.J.); edvard.govekar@fs.uni-lj.si (E.G.)
* Correspondence: primoz.potocnik@fs.uni-lj.si; Tel.: +386-1-4771-605

Abstract: In this study, a genetic algorithm-based laser beam (LB) path optimization method is presented to improve laser-based additive manufacturing (LBAM). To emulate the LBAM process, LB irradiation of a thin metal substrate is applied. The LB path generation is formulated as the search for the optimal sequence of LB irradiation into the cells on the substrate that minimizes the fitness function, which is composed of two components, i.e., thermal fitness and process fitness. The thermal fitness is expressed by the average thermal gradient, and a simple thermal model is developed to simulate the effects of laser-induced heat input on the temperature distribution in the substrate. The process fitness regulates the suitability of the proposed LB path for the implementation of the LBAM process. In addition to standardized tool paths (i.e., raster, spiral, etc.), novel LB path generators are proposed to define the initial population of LB path solutions. To implement a genetic algorithm-based LB path optimization, a framework is proposed, and custom initialization, crossover, and mutation operators are developed for application in LBAM. The effectiveness of the proposed approach is demonstrated through a simulation case study aiming to identify LB paths that minimize the fitness function and thus provide more suitable LB path solutions with respect to the defined fitness function. Compared with the traditional trial-and-error LB path formulations, the proposed approach provides an improved and automated method for an efficient laser beam path selection in LBAM.

Keywords: additive manufacturing; laser beam path; genetic algorithm; optimization

Citation: Potočnik, P.; Jeromen, A.; Govekar, E. Genetic Algorithm-Based Framework for Optimization of Laser Beam Path in Additive Manufacturing. *Metals* **2024**, *14*, 410. https://doi.org/10.3390/met14040410

Academic Editors: Xin Chen, Tao Zhang and Yongle Sun

Received: 12 March 2024
Revised: 28 March 2024
Accepted: 28 March 2024
Published: 29 March 2024

1. Introduction

Additive manufacturing (AM) has emerged as a swiftly advancing industrial paradigm, revolutionizing diverse industries with innovative solutions and applications [1]. AM empowers the creation of intricate, custom-designed components, and its digital-centric approach makes it one of the cutting-edge technologies of digital transformation. By directly translating digital designs into physical objects, AM reduces traditional manufacturing constraints and promotes innovation and flexibility. In addition, AM enables high material efficiency while minimizing waste, as only the materials necessary for manufacturing are used [2]. The minimal environmental footprint of this technology makes AM a sustainable, green solution in the context of Industry 4.0 [3]. Among AM technologies, laser-based additive manufacturing (LBAM) has gained significant attention for its versatility in processing a diverse range of materials, including metals, polymers, and ceramics. Notably, selective laser melting (SLM) and direct laser deposition (DLD) are preeminent AM processes involving the targeted melting and deposition of material layer by layer to construct intricate three-dimensional (3D) structures [4,5]. SLM can be used to produce complex parts with structures in the 100 μm range, while DED, with its high build rate and structures in the millimeter range, is used for larger, near-net-shaped components [3].

However, achieving the desired quality, accuracy, and mechanical properties in LBAM presents a challenge, predominantly due to the intricate interplay of material characteristics, process parameters, and part geometry. Common challenges of SLM and DLD are the demanding optimization of complex process parameters to reduce the porosity of the manufactured material, microstructural inconsistency, and dimensional inaccuracy. The latter, in addition to process intrinsic inaccuracies, results from residual stresses and the deformation of the parts, which are a consequence of suboptimal heat management. Residual stresses inherently arise during the complex thermo-mechanical phenomena due to the metal powder melting and solidification process, which involves rapid heating and cooling rates and large temperature gradients [6]. Therefore, one of the key challenges in laser-based AM revolves around controlling temperature distribution in the fabricated part during the deposition process. The laser-induced heat input can lead to nonuniform temperature distributions within the built part, resulting in undesirable effects such as residual stresses, deformations, and reduced mechanical properties of the final 3D-printed part [7,8]. To illustrate this effect, a simple experimental demonstration, formulated as an experimental motivation for this research, is provided in the next section.

For achieving a more homogeneous build part and improving the quality and accuracy of 3D metal printing, the temperature distribution in the printed part during the AM process is critical. This has spurred the emergence of novel machine learning-based methodologies aimed at addressing these complexities [9,10]. Robinson et al. [11] and Valente et al. [12] investigated the influence of scan strategy on residual stress, surface topography, and microstructure in AM of Ti-6Al-4V, providing essential insights into the complexities associated with laser scanning. Qi et al. [9] and Jin et al. [13] highlighted the application of neural network-based machine learning in AM. Wang et al. [10] provided a comprehensive review of the state-of-the-art machine learning applications, indicating a paradigm shift toward data-driven methodologies for optimizing AM processes.

Thermo-mechanical (TM) simulations, based on finite element (FE) numerical modeling, play a crucial role in understanding and optimizing the laser beam (LB) path in AM. Ren et al. [14] investigated various thermo-mechanical analyses for optimized path planning in LBAM processes. Comprehensive thermo-mechanical analyses, as demonstrated by Ren et al. [15], provide insights into the dynamic interplay between temperature and strain–stress distribution during the AM process. Results obtained using computer simulation based on a numerical model of the AM process contribute significantly to predicting and mitigating challenges such as residual stresses, distortion, and material defects [16]. The ability to simulate and analyze the thermo-mechanical behavior of materials during laser exposure provides the basis for the identification of optimal scanning patterns.

Nassehi et al. [17] introduced evolutionary algorithms for the generation and optimization of tool paths, showcasing their efficacy in exploring vast solution spaces. Various tool path planning approaches have been proposed to optimize the temperature properties of the build part [14,15,18], to predict the temperatures with an artificial neural network [19], and to introduce the optimized tool path into the AM process [20–22]. Zhou et al. used an evolutionary method for optimizing thermo-mechanical properties in wire-arc AM by generating optimized continuous tool paths [23]. Jia et al. [24] explored the influence of different scanning strategies on the thermo-mechanical characteristics of Ti-6Al-4V parts fabricated using SLM. Computer simulation and experimental tests were employed, and the results showed good consistency in the deformation characteristics between the numerical prediction and experimental observation. Recent advancements include the integration of deep learning for intelligent process monitoring [25] and reinforcement learning for tool-path design [26]. Boissier et al. [27] employed shape optimization tools for scanning path optimization, showcasing diverse strategies to enhance AM processes. Boissier et al. [28] also explored time-dependent scanning path optimization, introducing a dynamic dimension to the powder bed fusion additive manufacturing process. While significant progress has been made in the ongoing evolution of AM technologies, challenges persist in the domain of LB path optimization. Sun et al. [21] investigated novel patterns to reduce residual stress, addressing a critical challenge in achieving optimal part quality. Goh et al. [29] provided a comprehensive review of the challenges and potential applications of machine learning in 3D printing.

This study addresses the challenge of improving the dimensional accuracy of parts due to LBAM process-induced part distortion by providing a general framework for the optimization of the LB path. The proposed approach involves the development of an evolutionary optimization framework using a customized genetic algorithm (GA), which resembles and builds upon a previous study using an evolutional method in wire-arc additive manufacturing [23]. While continuous tool paths suitable for wire-arc AM are considered in [23], this study provides a framework where a process fitness regulates the degree of desired path continuity and therefore can be adapted to different LBAM processes. To demonstrate the proposed GA-based approach, fabrication of a single layer with an LBAM process was simulated using LB irradiation of a thin metal substrate. A simple thermal model was applied to simulate the effects of laser-induced heat input on the temperature distribution within the substrate during the LB irradiation. By using genetic algorithms for optimization, the limitations of traditional, time-consuming, trial-and-error tool-path formulations are overcome. The proposed approach provides an automated and efficient solution for finding an optimal LB path, leading to improved temperature distribution and increased suitability for the LBAM process implementation.

2. Experimental Motivation

The following experiment, shown in Figure 1, was conducted to demonstrate the motivation for this study. To mimic the fabrication of the single layer, a thin metal plate with dimensions of 120 × 120 mm and a thickness of 1.5 mm was exposed to laser irradiation on the LASERTEC 30 SLM machine (DMG MORI Additive Ltd, Bielefeld, Germany) without the presence of the powder material. The irradiation area of 90 mm × 90 mm on the plates was divided into $N_c \times N_c = 20 \times 20$ cells of 4.5 mm × 4.5 mm. The order of laser irradiation into the cells followed different LB path strategies, such as spiral-out, zigzag, and spiral-in, and intra-cell scanning was performed with a zigzag strategy. All the plates received the same amount of laser irradiation, yet in different orders of visited cells representing the LB path. Figure 1 shows: (a) the experimental setup with a plate fixed in the SLM machine, (b) an example of the processed plate with visible cells that received laser irradiation, (c) a metal plate before laser irradiation, and (d) a deformed metal plate after laser irradiation. The metal plate properties and dimensions are summarized in Table 1, and the laser parameters used in the experiments are shown in Table 2.

After the irradiation of the metal plate, using the selected LB paths (spiral-out, zigzag, spiral-in) as shown in Figure 2 (top), the plates were removed from the SLM machine and measured for mechanical deformation using the digital image correlation (DIC) system. The results of DIC measurement, after postprocessing and filtering out the plate pre-deformation, revealed very different deformation shapes caused by the different beam paths, as shown in Figure 2 (bottom).

We can observe considerable differences in the deformation shapes of the plates irradiated with spiral-in and spiral-out LB paths, deforming in opposite directions. The zigzag LB path results in less deformation and a smoother plate surface. The presented results of the significant influence of the LB path on the resulting thermally induced deformation of the plates provide the motivation to propose in this study a methodology for the optimization of LB paths.

Table 1. Metal plate properties and dimensions.

Property	Value
Material	AISI 304
Dimensions	120 mm × 120 mm
Thickness	1.5 mm
Clamping rail width	10 mm
Active irradiation area	90 mm × 90 mm
Partitioning of the irradiation area	20 × 20 square cells
Area of each cell	4.5 × 4.5 mm

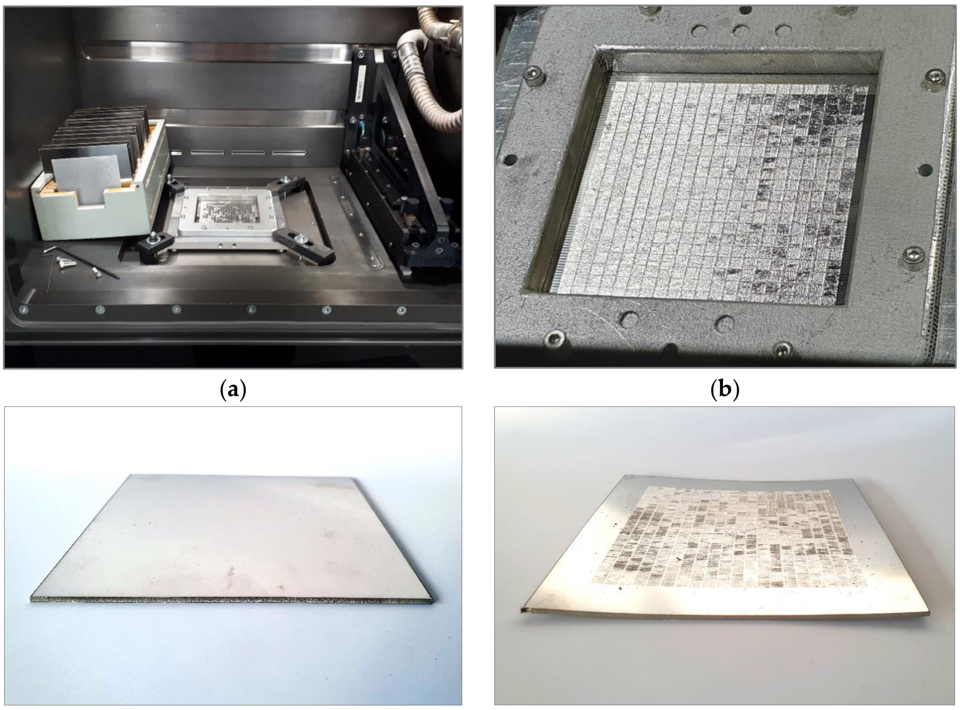

(**a**) (**b**) (c) (**d**)

Figure 1. (**a**) Experimental setup for examining the influence of the LB path on the metal plate deformation; (**b**) processed plate with visible cells that received laser irradiation; (**c**) metal plate before laser irradiation; (**d**) deformed metal plate after laser irradiation.

Table 2. Laser parameters.

Property	Value
Laser power	200 W
Scanning speed	1.2 m/s
Beam diameter	80 µm
Intra-cell scanning strategy	zigzag
Hatch distance	0.1 mm

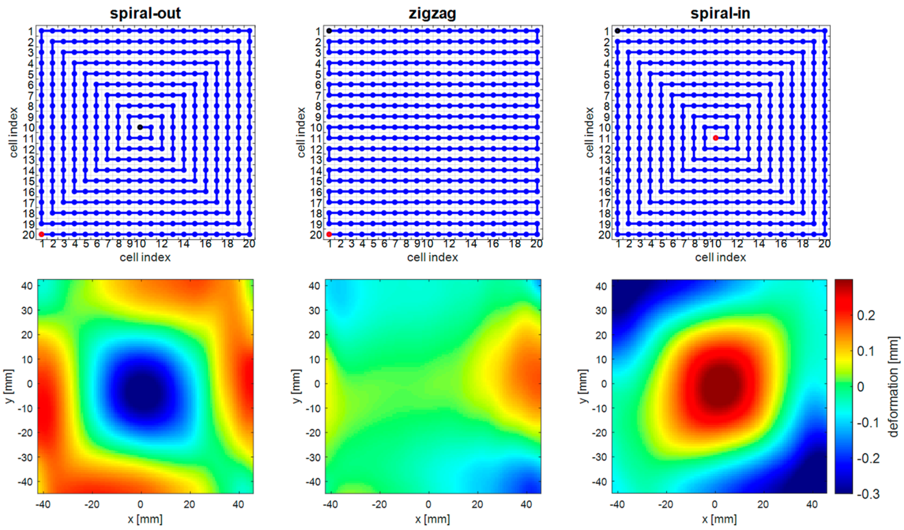

Figure 2. Experimental results of measured deformation of metal plates (**bottom**) that received laser irradiation according to different LB paths (**top**).

3. Methods

3.1. Overview of the Methods and Optimization Approach

This research is focused on laser-based additive manufacturing. The study demonstrates the optimization of LB path solutions in laser-based AM with the aim of achieving thermally more homogeneous properties, which in turn reduces the deformation of the fabricated part. The study considers only single-layer fabrication; however, the extension to multilayer deposition is possible by taking into account the heat distribution of the previous layers. For a simplified emulation of the laser-based AM process, the simulation setup includes a substrate (metal plate), which is irradiated by the LB. Due to the effects of the laser-induced heat input, the substrate may be subject to undesirable deformation. In this study, a simple thermal model was developed to simulate the effect of laser irradiation. The model does not consider the fusion of a powder layer or its direct deposition and melting by a laser and provides only the thermal response of the substrate due to the laser-induced heat input. As such, the thermal model provides a simplified simulation tool used in a defined fitness function, which is needed for the implementation of genetic algorithm-based optimization. The fitness function is designed to minimize the average thermal gradient on the substrate during the laser irradiation process and to take into account the suitability of the AM process-specific limitations of the tool path. The following sections explain the formulation of the tool path and the thermal model, and then, the optimization approach is described in more detail. The latter includes the development of an optimizer based on a genetic algorithm with custom operators for the initialization of the population, crossover, and mutation.

3.2. Tool Path Formulation

The substrate, i.e., the build plate in the case of LBAM, is partitioned into a grid of $N_c \times N_c$ cells (C), whereby each cell C represents a small unit as a sub-grid of $N_s \times N_s$ sub-cells (S). The physical dimensions of the cells C and S are determined by the parameters of the LBAM process used; e.g., when using the SLM method, each sub-cell S in the $N_s \times N_s$ cell has dimensions of approximately 0.1 mm × 0.1 mm (hatch distance in Table 2). The internal scanning of the individual cells C (i.e., the intra-cell scanning path) is determined by one of the standard scanning patterns (e.g., raster or zigzag). The size of cells C should be small with respect to the size of the processed area covered by the $N_c \times N_c$ cells so that the LB path optimization problem can be formulated in terms of the selection of a proper sequence within the set of $N_c \times N_c$ cells C and not in terms of optimizing the individual cells C.

An example of presenting an LB path in $N_c = 5$ cell C topology with $N_s = 4$ sub-cell S topology is shown in Figure 3. Each cell C is scanned internally with a zigzag pattern (Figure 3 left), and the order of cells C from 1 to 25 (Figure 3 center) determines the spiral-in irradiation sequence of the top-level topology, shown in Figure 3 (right), where black and red dots indicate the starting and ending cells. By keeping the dimension of the intra-cell topology small, the optimization problem can be formulated as the search for the optimal sequence of $N_c \times N_c$ cell irradiation that minimizes the fitness function.

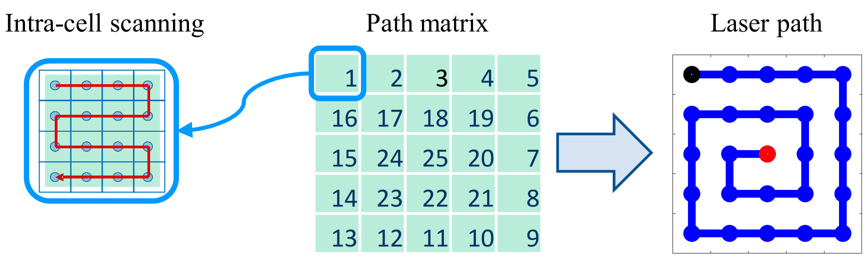

Figure 3. An example of a spiral-in LB path in $N_c \times N_c = 5 \times 5$ cell topology with $N_s \times N_s = 4 \times 4$ intra-cell topology, represented by a zigzag intra-cell LB scanning pattern (**left**), path matrix (**middle**), and spiral-in LB path (**right**).

3.2.1. Matrix Path Representation

As presented above, the basic format of the LB path representation is a matrix of the same size ($N_c \times N_c$) as the substrate (i.e., the build plate), with elements of the matrix representing the subsequent order of cells C on the build plate. For the example in Figure 3, the LB path p_1 is represented by the matrix as follows:

$$p_1 = \begin{bmatrix} 1 & 2 & 3 & 4 & 5 \\ 16 & 17 & 18 & 19 & 6 \\ 15 & 24 & 25 & 20 & 7 \\ 14 & 23 & 22 & 21 & 8 \\ 13 & 12 & 11 & 10 & 9 \end{bmatrix}. \quad (1)$$

However, to provide the description of an LB path for an arbitrary geometry of the layer shapes, this study introduces the design 'mask' operator, which defines which cells of the build plate are to be scanned with a selected scanning pattern and which cells remain unscanned. The mask operator is defined as the matrix of the size ($N_c \times N_c$) of the build plate, with ones denoting scanned cells and zeros denoting unscanned cells. An example of a simple 'L' mask and a possible LB path matrix p_2 (LB path sequence contains available cells only) can be expressed as follows:

$$\text{mask} = \begin{bmatrix} 1 & 1 & 1 & 0 & 0 \\ 1 & 1 & 1 & 0 & 0 \\ 1 & 1 & 1 & 0 & 0 \\ 1 & 1 & 1 & 1 & 1 \\ 1 & 1 & 1 & 1 & 1 \end{bmatrix}, \quad p_2 = \begin{bmatrix} 1 & 10 & 19 & 0 & 0 \\ 2 & 9 & 18 & 0 & 0 \\ 3 & 8 & 17 & 0 & 0 \\ 4 & 7 & 16 & 11 & 12 \\ 5 & 6 & 15 & 14 & 13 \end{bmatrix} \quad (2)$$

The design mask operator, the path matrix, and the corresponding laser scanning path are shown in Figure 4. In this example, the LB path consists of two segments (blue and red lines), which together constitute the complete LB path.

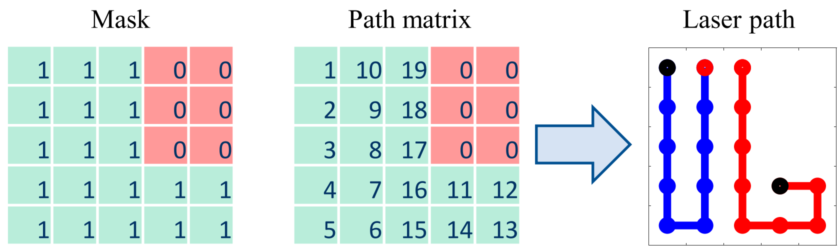

Figure 4. The design mask operator, the LB path matrix (p_2), and the corresponding LB path in ($N_c \times N_c$) = (5 × 5) build plate cell topology.

3.2.2. String Path Representation

For the manipulation of LB paths in a genetic algorithm, the LB paths must be represented by strings s_i, which is accomplished by the following transformation:

1. All the cells C (including the unscanned cells) in the path matrix are enumerated in the sequential order r, enumerating the cells C in the top-down and left-to-right order, as follows:

$$r = \begin{bmatrix} 1 & 2 & 3 & 4 & 5 \\ 6 & 7 & 8 & 9 & 10 \\ 11 & 12 & 13 & 14 & 15 \\ 16 & 17 & 18 & 19 & 20 \\ 21 & 22 & 23 & 24 & 25 \end{bmatrix} \quad (3)$$

2. The LB path representation is then expressed as the string of sequentially visited cells (according to the order matrix r). For the examples presented by Equations (1) and (2), the LB paths p_1 and p_2 can be expressed as strings s_1 and s_2, as follows:

$$s_1 = [1\ 2\ 3\ 4\ 5\ 10\ 15\ 20\ 25\ 24\ 23\ 22\ 21\ 16\ 11\ 6\ 7\ 8\ 9\ 14\ 19\ 18\ 17\ 12\ 13], \quad (4)$$

$$s_2 = [1\ 6\ 11\ 16\ 21\ 22\ 17\ 12\ 7\ 2\ 19\ 20\ 25\ 24\ 23\ 18\ 13\ 8\ 3]. \quad (5)$$

Notice that the string s_2 is shorter than s_1 due to the design mask, which excludes unscanned cells. The string representation s_i of an LB path is then applied in genetic algorithm-based operators. Nevertheless, both representations, matrix p_i and strings s_i, are equal and can be converted from one to the other. In the case of a design mask with zero elements, the conversion from a string into a matrix requires mask information and the enumerating order matrix r.

3.3. Thermal Model

To determine the thermal response of the irradiated substrate and the corresponding thermal fitness for the generated tool paths, a two-dimensional finite-volume heat conduction model of the LB irradiated substrate was formulated. The volume of the substrate was divided into $N_\mathrm{c} \times N_\mathrm{c}$ control volumes. In each control volume, the conservation of energy was satisfied:

$$\rho c \frac{dT}{dt} = \frac{\partial}{\partial x}\left(k\frac{\partial T}{\partial x}\right) + \frac{\partial}{\partial y}\left(k\frac{\partial T}{\partial y}\right) + S \quad (6)$$

To keep the model simple, adiabatic boundary conditions, uniform temperature T in the z direction, and constant properties of the AISI 304 substrate were assumed: density $\rho = 7900\ \mathrm{kg/m^3}$, specific heat $c = 480\ \mathrm{J/(kg\ K)}$, and thermal conductivity $k = 15\ \mathrm{W/(m\ K)}$ [30]. The choice of the substrate material (AISI 304) was motivated by the versatile applicability of this cost-effective stainless-steel alloy known for its corrosion resistance, mechanical strength, and ease of fabrication.

To emulate the LBAM process by LB irradiation of the substrate, a uniform volumetric heat source S was applied to the control volumes according to the tool path. The model was solved numerically using a tridiagonal matrix algorithm [31] with a fully implicit time scheme, resulting in a time-dependent temperature field $T(x, y, t)$. This thermal model is applied in our simulations for the calculation of temperature gradients, which constitutes the first part of the fitness function in the proposed optimization framework.

Figure 5 shows simulation examples for different LB paths (minNextTemp, spiral-out, raster) in the ($N_\mathrm{c} \times N_\mathrm{c}$) = (20 × 20) cell topology. The temperature distribution ($T_{t\,=\,200\ \mathrm{s}}$) at the end of the irradiation of the substrate with the LB paths is shown (bottom graphs) and reveals that different LB paths result in different temperature distributions within the substrate. The minNextTemp LB path is temperature optimized (explained in the next section); namely, the next irradiated cell is always the one with the lowest temperature. This reduces the temperature gradient within the substrate, which is also visible as a more homogeneous temperature field. The spiral-out LB path results in a less homogeneous temperature field at the end of the substrate irradiation, and the raster LB path accumulates even more heat at the end of the laser beam irradiation of the substrate.

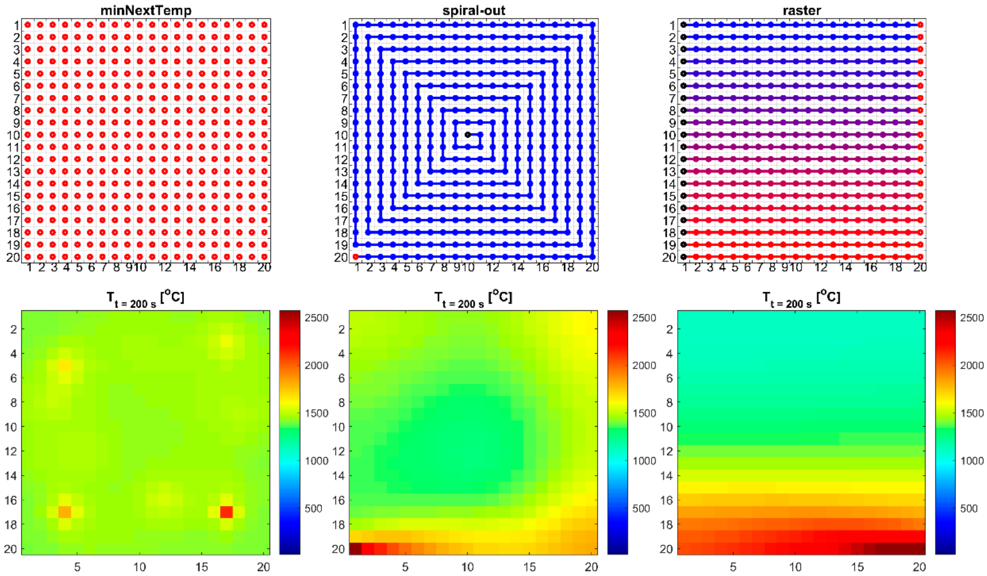

Figure 5. Examples of simulated temperature distributions for different LB paths (minNextTemp, spiral-out, raster) in the ($N_c \times N_c$) = (20 × 20) cell-substrate topology, at the end ($T_{t\,=\,200\,\mathrm{s}}$) of the laser beam irradiation of the substrate.

3.4. Genetic Algorithm

The genetic algorithm (GA) provides a global optimization solver for smooth or non-smooth optimization problems with any type of constraint [32]. It is a stochastic, population-based algorithm that searches randomly by crossover and mutation among population members. As schematically shown in Figure 6, the algorithm starts by creating an initial population of solutions, and then this population of individual solutions is repeatedly modified by crossover and mutation operators. At each step, the genetic algorithm selects individuals from the current population to be parents and uses them to produce children for the next generation. The fitness of individual solutions is evaluated by the fitness function. Over successive generations, the population evolves toward an optimal solution. GA-based methods have been proposed for solving various challenges in AM [13,33–35]. In this study, customized GA operators for LB path optimization are proposed and described in the following sections.

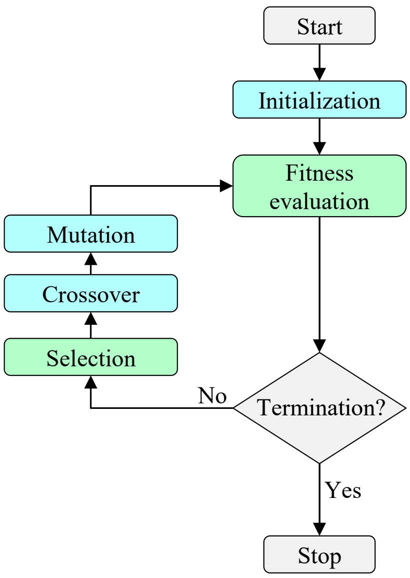

Figure 6. Schematic presentation of the flow of operation of a genetic algorithm.

3.4.1. Initialization

For the initial population of LB path solutions, in addition to a set of standardized LB paths (such as raster, zigzag, spiral, etc.), we propose specialized LB paths defined by a stochastic-based search generator, denoted as 'rand-worm', and two temperature-optimized LB path generators.

3.4.2. Rand-Worm Path Generator

This stochastic-based LB path generator is designed to search for random and preferably long continuous paths within the available path design topology (determined by the design mask). The algorithm starts from a random starting cell and then tries to (randomly) progress in various directions to continue the LB path segment. This process is iterated and restarted several times, and the longest obtained LB path segment is saved. The algorithm then moves to the next (randomly chosen) available cell and repeats the path search for the next segment. The algorithm ends when all available cells have been visited and included in the LB path. The algorithm can be summarized as follows:

A. Repeat for N_{rw} iterations (e.g., $N_{\mathrm{rw}} = 100$)
   1. Start a new segment by randomly choosing an available starting cell (available within the design mask and not occupied).
      i. Add this cell to the LB path segment.
      ii. Randomly choose a direction (up, down, left, right).
      iii. If a cell in the chosen direction is available, move to this cell and add it to the LB path segment.
      iv. Continue with step ii until the max number of tries is exhausted.
   2. If the LB path is stuck, start a new segment (go to step 1).
   3. Exit if all cells (within the design mask) are occupied.

B. Finally, select from the N_{rw} generated solutions the best rand-worm solution based on the process fitness evaluation (this is optional but guarantees solutions with better process fitness).

The algorithm for stochastic-based LB path generation uses a variant of a random walk and tries to fill the empty cells defined by the design mask on the grid of $N_{\mathrm{c}} \times N_{\mathrm{c}}$ cells C while avoiding blocking itself. The algorithm optimizes the LB path by evaluating multiple random walks and keeping the best one.

3.4.3. Temperature-Optimized LB Path Generators

These two generators are aimed at optimizing thermal fitness. Based on the thermal model (Section 3.3) to simulate the thermal properties of the substrate during LB irradiation, the two LB path generators are defined with respect to the following criteria:

1. *MinNextTemp generator*—in each step of the LB path, this generator finds the available cell that has the minimal temperature (among all cells), and this cell is chosen as the next cell in the LB path.
2. *MedianNextTemp generator*—in each step of the LB path, this generator finds the available cell that has the most average (median) temperature (among all cells), and this cell is chosen as the next cell in the LB path.

These two generators usually yield very dispersed solutions where the LB path is composed of mutually disconnected cells, which raises a high penalty within the process fitness (due to the short lengths of LB path segments). Nevertheless, these two generators provide a benchmark for thermal fitness by approximately minimizing the temperature gradients and are therefore often the best solutions (concerning thermal fitness) among the initial population of LB path solutions.

3.4.4. Initialization Examples

Standard tool-path generators can be applied in various orientations, which is relevant for asymmetric printing designs. The initial population can be populated with an arbitrary number of additional stochastic rand-worm solutions. The composition of the initial population thus consists of 12 standard tool path solutions, 2 temperature-optimized solutions, and additional rand-worm solutions (for example, 10 more rand-worm solutions), as follows:

- Raster (four orientations);
- Raster up-down (two orientations);
- Zigzag (four orientations);
- Spiral (two orientations, in and out);
- Temperature optimized (min, median);
- Rand-worm (arbitrary number of generated solutions).

Some examples of the initial population for the $N_c \times N_c = 20 \times 20$ cell substrate with an asymmetrical '9' design mask are shown in Figure 7. In the case of a symmetric design mask, different raster or zigzag orientations do not provide different LB path solutions (due to the symmetry of the design), but in the case of asymmetrical designs (as shown in Figure 7), the different orientations provide different LB path solutions (in terms of thermal properties). To show the progression of the LB path, the path is denoted with blue for the first deposited segment, red for the last segment, and shades of purple for the intermediate segments. For each segment, the black dot denotes the laser start, and the red dot denotes the laser end, i.e., the end of the segment before the LB moves to the next segment of the LB path.

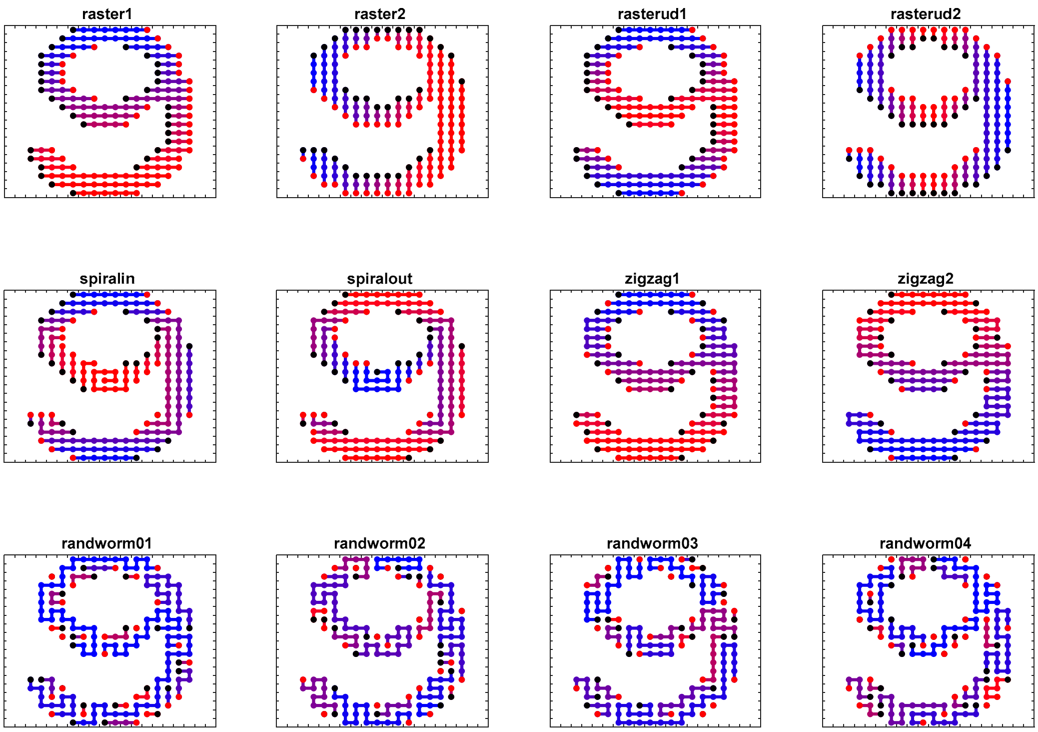

Figure 7. Examples of the initial population of LB paths for the $N_c \times N_c = 20 \times 20$ cell substrate with an asymmetrical '9' design mask.

3.4.5. Fitness Function

The fitness function J in GA optimization is required to provide the evaluation of LB path solutions. In this study, the fitness function is designed to minimize the average thermal gradient during the laser irradiation process and to regulate the suitability of the tool path for the AM process implementation. Consequently, the fitness function J in this study is composed of two components, namely:

1. Thermal fitness (J_{thermal}),
2. Process fitness (J_{process}).

The first component denotes the homogeneity of thermal distribution within the substrate, which consequently influences the substrate and causes its deformation. This fitness component is expressed as an average temperature gradient across the substrate and is averaged over the irradiation, i.e., deposition time, as follows:

$$J_{\mathrm{thermal}} = \mathrm{mean}(\mathrm{grad}(T)) \tag{7}$$

Low values of J_{thermal} correspond to overall low thermal gradients in the substrate, i.e., the build part, which results in fewer undesirable effects such as residual stresses, deformations, and reduced mechanical properties [7,8]. The second component of the fitness function evaluates the properties of the particular LB path solutions with respect to the AM process features and constraints. Although different LBAM processes have different characteristics and requirements to be fulfilled for their optimal performance, usually the following properties are desirable:

- A small number N_{up} of LB stops (with repositioning to a new location),
- A small number N_{singles} of single cells (just one deposition cell without continuation),
- Long LB path segments, which can be expressed through statistics such as the following:
  - L_{minSeg} (length of the shortest segment),
  - L_{meanSeg} (average length of segments).

These properties are combined in our study in the following process fitness:

$$J_{\mathrm{process}} = (N_{\mathrm{up}} + N_{\mathrm{singles}}) \,/\, (L_{\mathrm{minSeg}} + L_{\mathrm{meanSeg}}) \tag{8}$$

Low values of J_{process} are preferred to guarantee long, continuous LB paths. Finally, the multi-objective fitness function is defined as a combination of thermal and process fitness, as follows:

$$J = J_{\mathrm{thermal}} + \alpha\, J_{\mathrm{process}} \tag{9}$$

with weight α (in our study, set to $\alpha = 1$) denoting the ratio between thermal and process fitness. Based on the interpretation of the values of J_{thermal} and $J_{\mathrm{process},}$ the lower J means better overall performance of the LBAM process.

Examples of calculated values of the components of fitness functions for the previously shown LB paths (minNextTemp, spiral-out, and raster) in the $N_c \times N_c = 20 \times 20$ cell topology (Figure 5) are presented in Figure 8. The minNextTemp path provides the best thermal fitness (overall minimal thermal gradient). However, due to many interruptions of the LB path and changes in the location of the start of the consequent segment of the LB path, it is not suitable for the LBAM process implementation and therefore raises a high penalty in the process fitness. The spiral-out and raster paths are both excellent in terms of process suitability, but the raster path is thermally more suitable and therefore wins the overall fitness, with a value of $J = 44.3$.

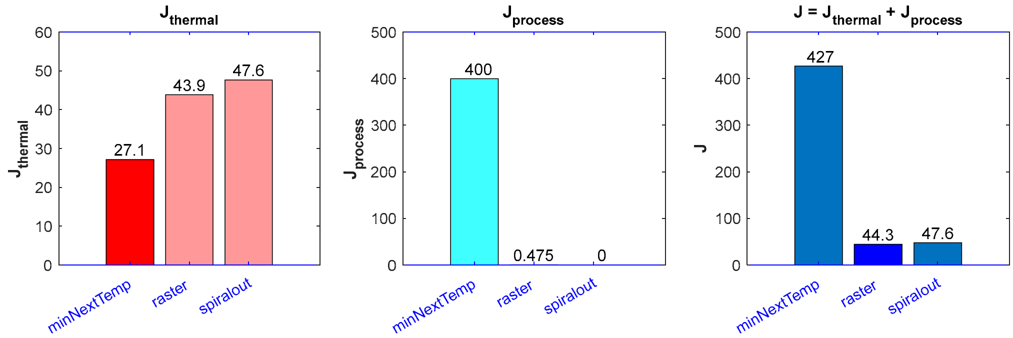

Figure 8. Examples of calculated component values J_{thermal} (**left**) and J_{process} (**middle**) of the fitness function J (**right**) for the minNextTemp, spiral-out, and raster LB paths.

3.4.6. Crossover Operator

The crossover operator in a genetic algorithm is a fundamental genetic operator used to combine genetic information from two parent solutions. It involves selecting specific genetic material, i.e., segments from the LB paths (in string presentation) from each parent, and exchanging it to create one or more offspring. This mimics the process of genetic recombination in biological reproduction, where traits from both parents are passed on to their offspring. The crossover operator helps the algorithm explore the solution space by generating diverse offspring, potentially producing individuals with improved fitness compared with their parents. In this study, the crossover operator performs the crossover operation between two parents, represented as LB path strings s_1 and s_2, to generate a new LB path offspring s_3.

Figure 9 illustrates the crossover operation and shows an example of the crossover between two parent LB paths on an $N_c \times N_c = 10 \times 10$ substrate with a full design mask and the corresponding effective length of the path strings $L_p = 100$ (denoting the number of available cells of the LB path strings). Original parents s_1 and s_2, representing the spiral-in and zigzag LB paths, are shown in Figure 9a,b, and the crossover operation is described below.

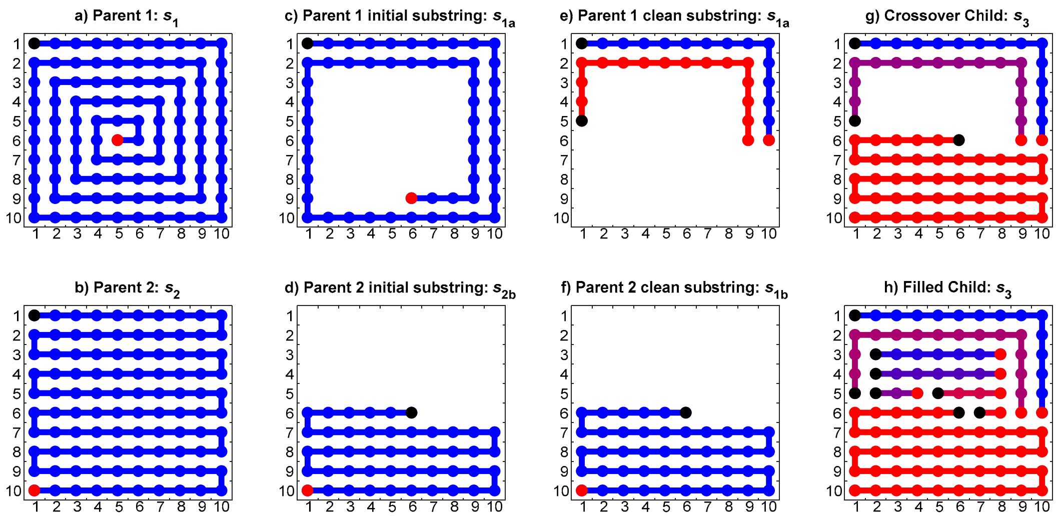

Figure 9. The crossover operation combines the selected LB path segments of parents s_1 and s_2 into a child s_3.

The crossover operation involves the following steps:

1. Based on the GA selection policy, pick two parent paths s_1 and s_2 (Figure 9a,b).
2. Define the crossover point N_{cross}.

- The effective length of the path strings L_p is calculated by taking into account the mask (the number of mask elements that are set to one).
- The crossover point N_{cross} is randomly selected within the effective length of the path strings. In Figure 9, the crossover point is selected as N_{cross} = 54.

3. Split the parent path strings at the crossover point $N_{cross.}$
    - Parent path strings s_1 and s_2 are split at crossover point N_{cross} to generate two sub-strings [s_{1a}, s_{1b}] and [s_{2a}, s_{2b}] (sub-strings s_{1a} and s_{2b} are shown in Figure 9c,d).
4. Crossover matching
    - The crossover matching starts by taking the first substring of s_1, namely s_{1a}, and the second substring of s_2, namely s_{2b}, to compose the initial offspring s_3 = [s_{1a}, s_{2b}].
5. The next step is cleaning the offspring s_3 of duplicate elements (except for the elements corresponding to 0 in the mask).
    - Case 1: If duplicates are found, they are progressively removed from the offspring string s_3 until no duplicate cells are found in s_3 (clean substrings [s_{1a}, s_{2b}] are shown in Figure 9e,f).
    - Case 2: If no duplicates are found, the crossover operation is successful, and the function returns the new offspring s_3 (as illustrated in Figure 9g).
6. Finally, missing elements are filled by one of the available LB path generators (randomly chosen) to generate the final (filled) offspring s_3 (Figure 9h).

After the completed crossover operation, the child s_3 may be selected also for a mutation (as described below), and the new LB path solution will then be evaluated by the fitness function and eventually, depending on the fitness value, propagated in the GA evolution.

3.4.7. Mutation Operator

The mutation operator is responsible for introducing diversity into the population by randomly altering the genetic material of the selected individual (parent) to generate new offspring. The mutation implementation in this study is illustrated in Figure 10 (on an $N_c \times N_c = 10 \times 10$ substrate) and creates a new offspring s_2 from a parent s_1 as follows:

1. Select a parent path s_1 (Figure 10a).
2. Randomly choose a mutation start point (N_{mut1}) and endpoint (N_{mut2}).
3. The mutation operator deletes the path within the selected interval [N_{mut1}, N_{mut2}] (Figure 10b).
4. Finally, deleted elements are filled by one of the available and randomly chosen LB path generators to create the filled child s_2 (Figure 10c).

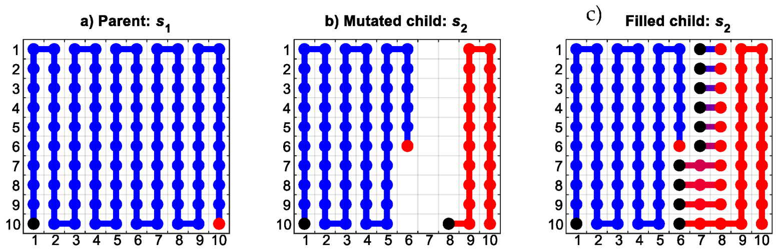

Figure 10. In this example, the mutation operation is applied to a parent s_1 (**a**) to obtain the mutated child s_2 (**b**), and then the LB path generator is applied to fill the missing cells and generate the filled child s_2 (**c**).

Thus, the mutation operator generates a new solution by randomly mutating a segment of the parent and filling in the gaps. This is a common technique in genetic algorithms, where small, random changes are made to a solution to explore the search space and potentially find better solutions.

4. Simulations and Results

This section presents a few thermal model simulation-based results of the operation of the proposed LB path optimization framework. The same metal plate properties and dimensions as summarized in Table 1 were used for the simulations, and the configuration of the thermal model (laser parameters) and the parameters defining the behavior of the GA-based optimization of the tool path are summarized in Table 3. Simulations were performed with various mask designs on an $N_c \times N_c = 20 \times 20$ substrate of AISI 304 material (which was also used in the case of the motivation experiment presented in Section 2).

The simulation results show the operation of the proposed path optimization framework, taking into account the formulated fitness function J (Equation (7)). Therefore, these results serve primarily as a basis and proof of concept for the optimization framework, which will be combined in further research with more detailed thermo-mechanical simulations, including material deformation and experimental validation of the simulation results.

Three simulation examples are presented in the following: the 'Y' mask, the 'H' mask, and the '9' mask. For each case, the resulting optimized path is shown. For the case of a '9' mask, to illustrate the fitness evaluations, the overall fitness, thermal fitness, and process fitness values are presented for the initial population and the final optimized path.

Table 3. Configuration of the thermal model (laser parameters) and the parameters defining the behavior of GA-based optimization of the LB path.

Laser parameters	
Laser power	200 W
Time for one-cell deposition	0.5 s
Percentage of time on each cell when the laser is active	100%
GA parameters	
Number of generations	500
Max. number of stalled generations	100
Number of iterations of searching for the fittest rand-worm path	20
Number of crossover attempts (to obtain a valid path)	100
Number of mutation attempts (to obtain a valid path)	100

Optimized Paths

Based on the initial population of paths for the substrate $N_c \times N_c = 20 \times 20$ with 'Y', 'H', and '9' masks, a simulated optimization was performed by using the thermal model and the proposed genetic algorithm-based optimization framework. Examples of the considered initial population for the '9' mask are shown in Figure 7. The resulting optimized paths of the simulated evolution for Y', 'H', and '9' masks are shown in Figure 11.

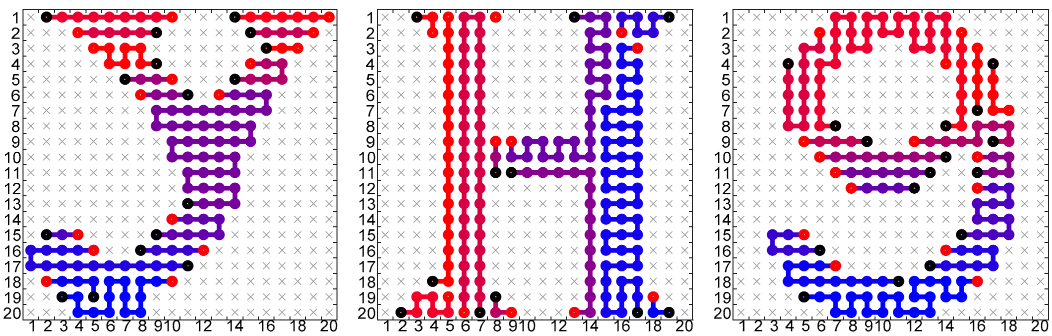

Figure 11. Simulation results of optimizing the tool path for the 'Y', 'H', and '9' masks on a 20×20 square cells substrate.

In all the cases, the GA-optimized LB paths improve the overall fitness J, which amounts to 27.6, 22.1, and 24.1 for the 'Y', 'H', and '9' masks, respectively. The fitness evaluations for the '9' mask, for the complete initial population of 24 LB path solutions and the optimized GA result, are shown in Figure 12. As evident in the considered case, the resulting GA-optimized LB path provides the best overall fitness, J = 24.1, which is composed of thermal fitness J_{thermal} = 23.2 and process fitness J_{process} = 0.972.

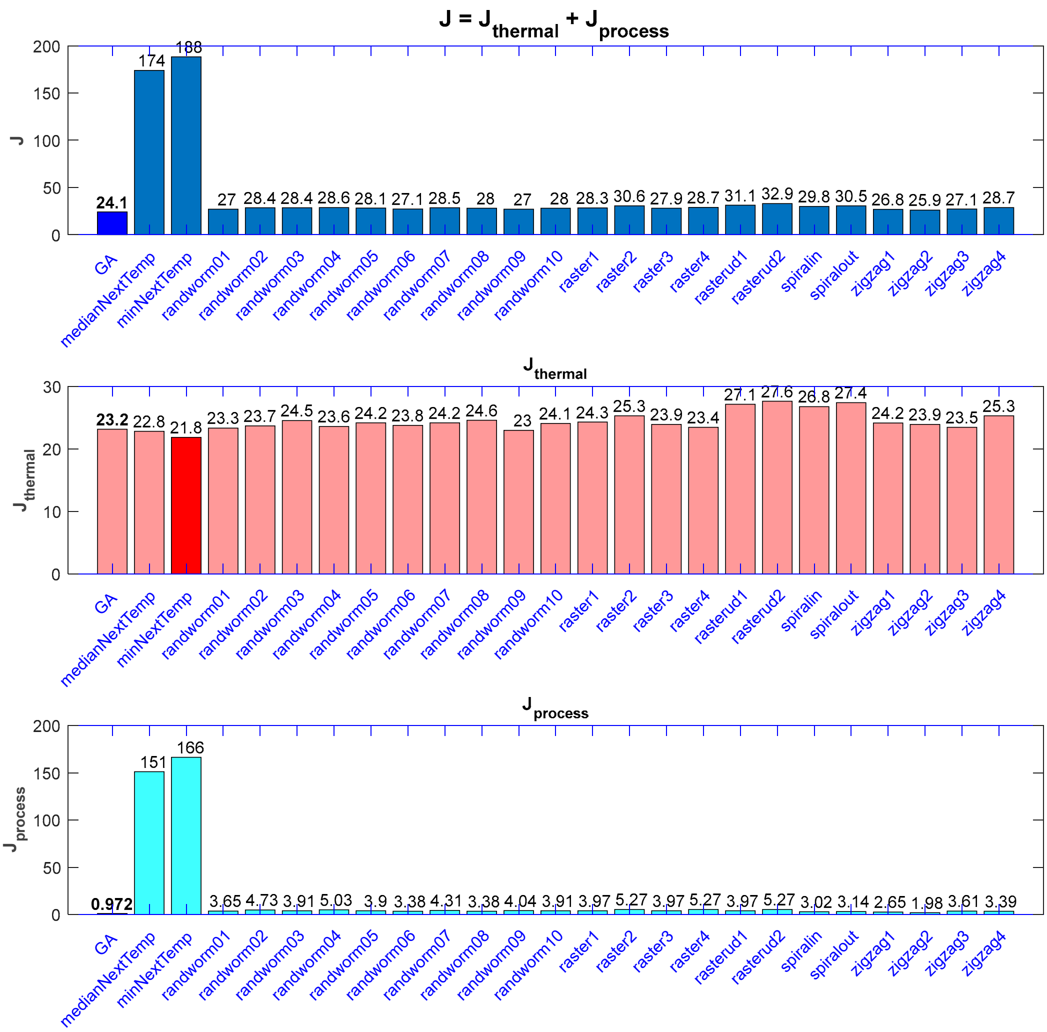

Figure 12. Fitness evaluations ('9' mask on an $N_c \times N_c$ = 20 × 20 substrate) for a complete initial population and the simulation result (GA), including the overall fitness J, thermal fitness J_{thermal}, and process fitness J_{process}.

5. Conclusions

This study provides a framework for genetic algorithm-based optimization of LB paths for improving laser-based additive manufacturing. The novelties of the proposed approach include the 'rand-worm' generator for generating stochastic-based laser beam paths and the development of custom GA operators (initialization, crossover, mutation) that are suited to operate with laser beam paths. The laser paths are encoded in a matrix or string format, the latter being appropriate for the GA optimization operations. The arbitrary path geometries can be defined by using the mask operator. The specifics of the process can be addressed by regulating the fitness function, which in this study consists of a thermal and process fitness. Thus, the multi-objective fitness function can be adjusted to correspond to different process requirements; therefore, this study provides a general GA-based optimization framework suitable for further research of optimal tool path methods for additive manufacturing.

The study presents simulated results, based on applying a simple thermal mode to simulate the effects of laser-induced heat input on the temperature distribution within the substrate. The LB path optimization is formulated as the search for the optimal sequence of cell depositions that minimize the fitness function. In the presented cases, thermal fitness is expressed as the average thermal gradient, and process fitness regulates the suitability of the proposed LB path for the selected AM process implementation. The simulation results (i.e., Figures 11 and 12) show that novel, innovative LB paths can be obtained with the GA-based optimization framework, and the resulting LB paths improve the fitness function and therefore represent potentially better solutions for the AM process.

The limitation of this study is the application of a simple thermal model, which does not accurately describe the heat transfer in a physical workpiece and consequently cannot provide predictions of realistic thermo-mechanical deformations caused by laser-based heat input. Therefore, future research will include more advanced thermo-mechanical simulation models, including temperature-dependent material properties, to provide a more accurate estimation of the thermal and mechanical loads in the workpiece during the laser-based AM process. This should provide a more accurate estimation of the expected thermo-mechanical deformations of the fabricated part and a basis for focused experiments with selected (and optimized) laser beam paths. The multi-objective fitness function for future experimental validation of the proposed GA-based LB path optimization will be extended to include, besides thermal gradients, various characteristics of the manufactured parts, such as deformation, porosity, metallographic properties, and mechanical properties.

This research contributes to the advancement of AM with a focus on LBAM and its applications in diverse industrial sectors by providing a flexible and automated GA-based approach to optimizing LB paths. Compared with the traditional trial-and-error LB path formulations, the proposed approach offers an improved and automated solution for determining an efficient LB path in LBAM. Further research will therefore include more realistic thermo-mechanical modeling and extensive experimental validation of the proposed GA-based optimization approach based on different LBAM processes, including SLM and DLD processes.

Author Contributions: Conceptualization, P.P., A.J. and E.G.; methodology, P.P., A.J. and E.G.; software, P.P. and A.J.; validation, P.P. and A.J.; investigation, P.P. and A.J.; resources, E.G.; data curation, P.P. and A.J.; writing—original draft preparation, P.P. and A.J.; writing—review and editing, P.P. and E.G.; visualization, P.P.; project administration, E.G.; funding acquisition, E.G. All authors have read and agreed to the published version of the manuscript.

Funding: This work was funded by ARIS—Slovenian Research and Innovation Agency—Research program P2-0241.

Data Availability Statement: The original contributions presented in the study are included in the article, further inquiries can be directed to the corresponding author.

Conflicts of Interest: The authors declare no conflicts of interest.

References

1. Madhavadas, V.; Srivastava, D.; Chadha, U.; Aravind Raj, S.; Sultan, M.T.H.; Shahar, F.S.; Shah, A.U.M. A Review on Metal Additive Manufacturing for Intricately Shaped Aerospace Components. *CIRP J. Manuf. Sci. Technol.* **2022**, *39*, 18–36. [CrossRef]
2. Blakey-Milner, B.; Gradl, P.; Snedden, G.; Brooks, M.; Pitot, J.; Lopez, E.; Leary, M.; Berto, F.; du Plessis, A. Metal Additive Manufacturing in Aerospace: A Review. *Mater. Des.* **2021**, *209*, 110008. [CrossRef]
3. Lupi, F.; Pacini, A.; Lanzetta, M. Laser Powder Bed Additive Manufacturing: A Review on the Four Drivers for an Online Control. *J. Manuf. Process.* **2023**, *103*, 413–429. [CrossRef]
4. Shamsaei, N.; Yadollahi, A.; Bian, L.; Thompson, S.M. An Overview of Direct Laser Deposition for Additive Manufacturing; Part II: Mechanical Behavior, Process Parameter Optimization and Control. *Addit. Manuf.* **2015**, *8*, 12–35. [CrossRef]
5. Thompson, S.M.; Bian, L.; Shamsaei, N.; Yadollahi, A. An Overview of Direct Laser Deposition for Additive Manufacturing; Part I: Transport Phenomena, Modeling and Diagnostics. *Addit. Manuf.* **2015**, *8*, 36–62. [CrossRef]
6. Nandhakumar, R.; Venkatesan, K. A Process Parameters Review on Selective Laser Melting-Based Additive Manufacturing of Single and Multi-Material: Microstructure, Physical Properties, Tribological, and Surface Roughness. *Mater. Today Commun.* **2023**, *35*, 105538. [CrossRef]
7. Zheng, Y.; Liu, F.; Gao, J.; Liu, F.; Huang, C.; Zheng, H.; Wang, P.; Qiu, H. Effect of Different Heat Input on the Microstructure and Mechanical Properties of Laser Cladding Repaired 300M Steel. *J. Mater. Res. Technol.* **2023**, *22*, 556–568. [CrossRef]

8. Reda Al-Sayed, S.; Elgazzar, H.; Nofal, A. Metallographic Investigation of Laser-Treated Ductile Iron Surface with Different Laser Heat Inputs. *Ain Shams Eng. J.* **2023**, *14*, 102189. [CrossRef]
9. Qi, X.; Chen, G.; Li, Y.; Cheng, X.; Li, C. Applying Neural-Network-Based Machine Learning to Additive Manufacturing: Current Applications, Challenges, and Future Perspectives. *Engineering* **2019**, *5*, 721–729. [CrossRef]
10. Wang, C.; Tan, X.P.; Tor, S.B.; Lim, C.S. Machine Learning in Additive Manufacturing: State-of-the-Art and Perspectives. *Addit. Manuf.* **2020**, *36*, 101538. [CrossRef]
11. Robinson, J.; Ashton, I.; Fox, P.; Jones, E.; Sutcliffe, C. Determination of the Effect of Scan Strategy on Residual Stress in Laser Powder Bed Fusion Additive Manufacturing. *Addit. Manuf.* **2018**, *23*, 13–24. [CrossRef]
12. Valente, E.H.; Gundlach, C.; Christiansen, T.L.; Somers, M.A.J. Effect of Scanning Strategy During SLM on Surface Topography, Porosity, and Microstructure of AM Ti-6Al-4V. *Appl. Sci.* **2019**, *9*, 5554. [CrossRef]
13. Jin, Z.; Zhang, Z.; Demir, K.; Gu, G.X. Machine Learning for Advanced Additive Manufacturing. *Matter* **2020**, *3*, 1541–1556. [CrossRef]
14. Ren, K.; Chew, Y.; Fuh, J.Y.H.; Zhang, Y.F.; Bi, G.J. Thermo-Mechanical Analyses for Optimized Path Planning in Laser Aided Additive Manufacturing Processes. *Mater. Des.* **2019**, *162*, 80–93. [CrossRef]
15. Ren, K.; Chew, Y.; Zhang, Y.F.; Bi, G.J.; Fuh, J.Y.H. Thermal Analyses for Optimal Scanning Pattern Evaluation in Laser Aided Additive Manufacturing. *J. Mater. Process. Technol.* **2019**, *271*, 178–188. [CrossRef]
16. Stathatos, E.; Vosniakos, G.C. Efficient Temperature Regulation through Power Optimization for Arbitrary Paths in Laser Based Additive Manufacturing. *CIRP J. Manuf. Sci. Technol.* **2021**, *33*, 133–142. [CrossRef]
17. Nassehi, A.; Essink, W.; Barclay, J. Evolutionary Algorithms for Generation and Optimization of Tool Paths. *CIRP Ann.—Manuf. Technol.* **2015**, *64*, 455–458. [CrossRef]
18. Ding, D.; Pan, Z.; Cuiuri, D.; Li, H. A Tool-Path Generation Strategy for Wire and Arc Additive Manufacturing. *Int. J. Adv. Manuf. Technol.* **2014**, *73*, 173–183. [CrossRef]
19. Farias, F.W.C.; da Cruz Payão Filho, J.; Moraes e Oliveira, V.H.P. Prediction of the Interpass Temperature of a Wire Arc Additive Manufactured Wall: FEM Simulations and Artificial Neural Network. *Addit. Manuf.* **2021**, *48*, 102387. [CrossRef]
20. Malekipour, E.; Valladares, H.; Shin, Y.; El-Mounayri, H. Optimization of Chessboard Scanning Strategy Using Genetic Algorithm in Multi-Laser Additive Manufacturing Process. *ASME Int. Mech. Eng. Congr. Expo. Proc.* **2020**, *84485*, 2A-2020. [CrossRef]
21. Sun, L.; Ren, X.; He, J.; Zhang, Z. Numerical Investigation of a Novel Pattern for Reducing Residual Stress in Metal Additive Manufacturing. *J. Mater. Sci. Technol.* **2021**, *67*, 11–22. [CrossRef]
22. Ramani, K.S.; He, C.; Tsai, Y.L.; Okwudire, C.E. SmartScan: An Intelligent Scanning Approach for Uniform Thermal Distribution, Reduced Residual Stresses and Deformations in PBF Additive Manufacturing. *Addit. Manuf.* **2022**, *52*, 102643. [CrossRef]
23. Zhou, Z.; Shen, H.; Lin, J.; Liu, B.; Sheng, X. Continuous Tool-Path Planning for Optimizing Thermo-Mechanical Properties in Wire-Arc Additive Manufacturing: An Evolutional Method. *J. Manuf. Process.* **2022**, *83*, 354–373. [CrossRef]
24. Jia, Y.; Zeng, C.; Xue, J. Scanning Strategy Optimization for the Selective Laser Melting Additive Manufacturing of Ti6Al4V. *Eng. Res. Express* **2023**, *5*, 015041. [CrossRef]
25. Li, X.; Siahpour, S.; Lee, J.; Wang, Y.; Shi, J. Deep Learning-Based Intelligent Process Monitoring of Directed Energy Deposition in Additive Manufacturing with Thermal Images. *Procedia Manuf.* **2020**, *48*, 643–649. [CrossRef]
26. Mozaffar, M.; Ebrahimi, A.; Cao, J. Toolpath Design for Additive Manufacturing Using Deep Reinforcement Learning. *arXiv* **2020**, arXiv:2009.14365. [CrossRef]
27. Boissier, M.; Allaire, G.; Tournier, C. Additive Manufacturing Scanning Paths Optimization Using Shape Optimization Tools. *Struct. Multidiscip. Optim.* **2020**, *61*, 2437–2466. [CrossRef]
28. Boissier, M.; Allaire, G.; Tournier, C. Time Dependent Scanning Path Optimization for the Powder Bed Fusion Additive Manufacturing Process. *CAD Comput. Aided Des.* **2022**, *142*, 103122. [CrossRef]
29. Goh, G.D.; Sing, S.L.; Yeong, W.Y. A Review on Machine Learning in 3D Printing: Applications, Potential, and Challenges. *Artif. Intell. Rev.* **2021**, *54*, 63–94. [CrossRef]
30. Incropera, F.P.; Dewitt, D.P. *Fundamentals of Heat and Mass Transfer*, 3rd ed.; Wiley: Hoboken, NJ, USA, 1990.
31. Patankar, S. *Numerical Heat Transfer and Fluid Flow*; CRC Press: Boca Raton, FL, USA, 1980.
32. Goldberg, D.E.; Holland, J.H. *Genetic Algorithms in Search, Optimization, and Machine Learning*; Addison-Wesley Professional: Hoboken, NJ, USA, 1989.
33. Vaissier, B.; Pernot, J.P.; Chougrani, L.; Véron, P. Genetic-Algorithm Based Framework for Lattice Support Structure Optimization in Additive Manufacturing. *CAD Comput. Aided Des.* **2019**, *110*, 11–23. [CrossRef]
34. Moussa, M.; ElMaraghy, H. A Genetic Algorithm-Based Model for Product Platform Design for Hybrid Manufacturing. *Procedia CIRP* **2020**, *93*, 389–394. [CrossRef]
35. Liu, N.; Ren, K.; Zhang, W.; Zhang, Y.F.; Chew, Y.X.; Bi, G.J.; Fuh, J.Y.H. An Evolutional Algorithm for Automatic 2D Layer Segmentation in Laser-Aided Additive Manufacturing. *Addit. Manuf.* **2021**, *47*, 102342. [CrossRef]